algorithms

MDPI

Article

Partial Discharge Data Augmentation and Pattern Recognition Method Based on DAE-GAN †

Xin Du [1], Jun Qi [1], Jiyi Kang [1], Zezhong Sun [2], Chunxin Wang [2] and Jun Xie [2,*]

[1] Alxa Power Supply Branch, Inner Mongolia Electric Power (Group) Co., Ltd., Alxa 750300, China; duxin1@impc.com.cn (X.D.); kangjiyi@impc.com.cn (J.K.)
[2] State Key Laboratory of New Energy Power System, North China Electric Power University, Baoding 071000, China; 220232213021@ncepu.edu.cn (Z.S.)
* Correspondence: junxie@ncepu.edu.cn
† This article is a revised and expanded version of a paper entitled Partial Discharge Data Augmentation and Pattern Recognition for Unbalanced and Small Sample Scenarios, which was presented at the 7th International Seminar on Computer Technology, Mechanical and Electrical Engineering (ISCME 2022) (Hangzhou, China).

Abstract: Accurate identification of partial discharge (PD) and its types is essential for assessing the operating conditions of electrical equipment. To enhance PD pattern recognition under imbalanced and limited sample conditions, a method based on a Deep Autoencoder-embedded Generative Adversarial Network (DAE-GAN) is proposed. First, the Deep Autoencoder (DAE) is embedded within the Generative Adversarial Network (GAN) to improve the realism of generated samples. Then, complementary PD data samples are introduced during GAN training to address the issue of limited sample size. Lastly, the model's discriminator is fine-tuned with augmented and balanced training data to enable PD pattern recognition. The DAE-GAN method is used to augment data and recognize patterns in experimental PD signals. The results demonstrate that, under imbalanced and small sample conditions, DAE-GAN generates more authentic PD samples with improved probability distribution fitting compared to other algorithms, leading to varying levels of enhancement in pattern recognition accuracy.

Keywords: partial discharge; data augmentation; DAE; GAN; DAE-GAN

Citation: Du, X.; Qi, J.; Kang, J.; Sun, Z.; Wang, C.; Xie, J. Partial Discharge Data Augmentation and Pattern Recognition Method Based on DAE-GAN. *Algorithms* **2024**, *17*, 487. https://doi.org/10.3390/a17110487

Academic Editor: Antonio Della Cioppa

Received: 29 August 2024
Revised: 17 October 2024
Accepted: 28 October 2024
Published: 1 November 2024

1. Introduction

Electrical equipment is a critical element of power systems, and its safety and stability have a significant effect on the overall reliability of system operations [1–3]. Proper identification of partial discharge (PD) and its various types is fundamental for evaluating the operational health of electrical equipment [4].

For effective pattern recognition, it is crucial to have a sufficient quantity of training samples with a well-balanced category distribution [5,6]. However, the available PD samples for electrical equipment are limited, and the category distribution is uneven [7,8]. The small sample size reduces the available information about the PD sample probability distribution, making it difficult to develop a reliable pattern recognition model. This imbalance causes the minority class samples to receive inadequate attention, resulting in poor recognition accuracy for these samples.

The current mainstream method for solving the problem of sample imbalance is to perform data augmentation on the sample [9]. In data augmentation methods, under-sampling [10], random over-sampling [11] (ROS), and the synthetic minority oversampling technique [12] (SMOTE) can lead to missing or biased probability distributions of the generated imbalanced samples, resulting in overfitting of the classifier. Sample generation methods based on deep learning have emerged in imbalanced sample oversampling methods in recent years [13,14]. Yang H et al. [15] utilized a Variational Autoencoder (VAE) for PD data matching. VAE-generated samples tend to be smooth but face challenges such

as inter-class blurriness and mode collapse, which limits the diversity of the generated data [16]. The Boundary Equilibrium Generative Adversarial Network (BEGAN) [17], utilizing an autoencoder as its discriminator along with a balancing strategy, allows for quick and stable convergence. While BEGAN generates PD samples that closely resemble the originals, issues like mode collapse and limited diversity persist. Zheng M et al. [18] applied the Conditional Wasserstein GAN with gradient penalty (CWGAN-GP) to augment transformer fault samples, using the Wasserstein distance as the objective function with a gradient penalty term. This approach effectively mitigates gradient vanishing and mode collapse and supports multi-class sample generation. However, CWGAN-GP struggles with slow convergence when generating high-dimensional samples, often leading to either overly sharp or noisy outputs. In comparison, models like VAE and BEGAN tend to produce more realistic samples. The currently proposed generative models aim solely at approximating the distribution of samples within the same class without utilizing the probabilistic information in the sample supplement set, indicating room for improvement in the accuracy of fitting the target distribution.

To enhance PD pattern recognition accuracy in scenarios with imbalanced and small sample sizes, this paper proposes a data augmentation and recognition method based on a Generative Adversarial Network integrated with a Deep Autoencoder (DAE-GAN) [19]. The approach uses denoised PD pulses as input and embeds a deep autoencoder into the sample generation process of CWGAN-GP. The DAE improves the realism of generated samples while addressing sample imbalance by creating additional PD samples. During training, complementary samples are introduced to utilize probabilistic information in the dataset, aiding in better probability distribution fitting and mitigating the small sample issue. The generated data is then used to fine-tune the discriminator, which serves as a classifier for PD pattern recognition. Experimental results indicate that the proposed method, under imbalanced and small sample conditions, significantly enhances sample authenticity, improves probability distribution fitting, and boosts PD pattern recognition accuracy.

2. Partial Discharge Test and Signal Preprocessing

Four discharge models are developed to simulate common transformer insulation defects: tip discharge, surface discharge, bubble discharge, and floating discharge [20]. The cardboard used for the tip, surface, and floating discharge models has a thickness of 2 mm, while the bubble discharge model consists of three layers of cardboard with thicknesses of 0.5 mm, 2 mm, and 0.5 mm. The dimensions and structures of the discharge models are illustrated in Figure 1 [21].

The partial discharge pulses were measured using the high-frequency current method [22], and the experimental circuit is shown in Figure 2. The experiments were conducted in an electromagnetic shielding room, and high-frequency partial discharge signals were collected from the grounding wire using the high-frequency current method. A synchronized acquisition card was employed to ensure the synchronization between the collected partial discharge signals and the reference voltage signals. After applying the target voltage, sampling began once the discharge signals stabilized. A triggered sampling method was used, where samples were collected when the discharge amplitude exceeded the trigger threshold. The sampling bandwidth was 100 MHz, and discharge signals over 100 power frequency cycles were continuously collected as long-term signal samples. In order to further improve the quality of the PD test signal, the research group proposes an adaptive weighted-frame fast sparse-representation denoising method [23], which has smaller amplitude error and waveform distortion and higher efficiency. This method is also used to denoise the partial discharge test samples. The single-pulse partial discharge was extracted using an adaptive double-threshold extraction method [24]. The time–domain waveforms of the four types of single-pulse partial discharge are shown in Figure 3 [21].

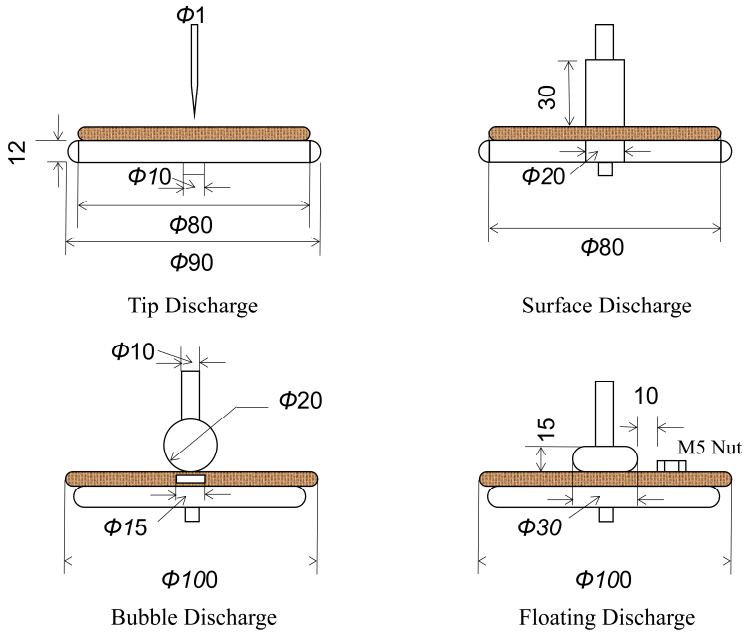

Figure 1. Partial discharge models [21].

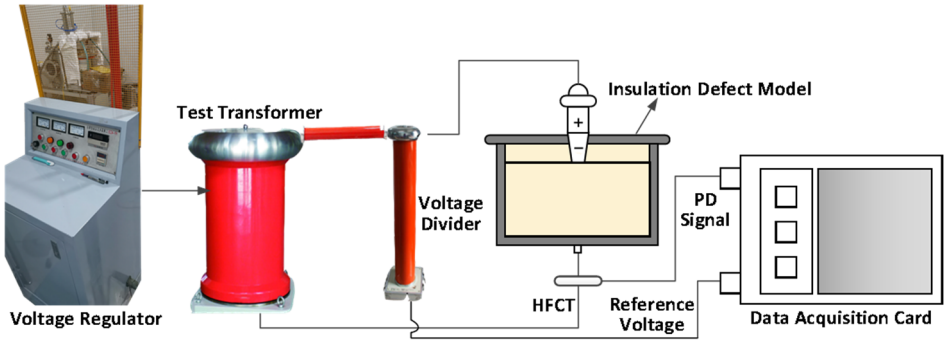

Figure 2. Experimental circuit wiring diagram.

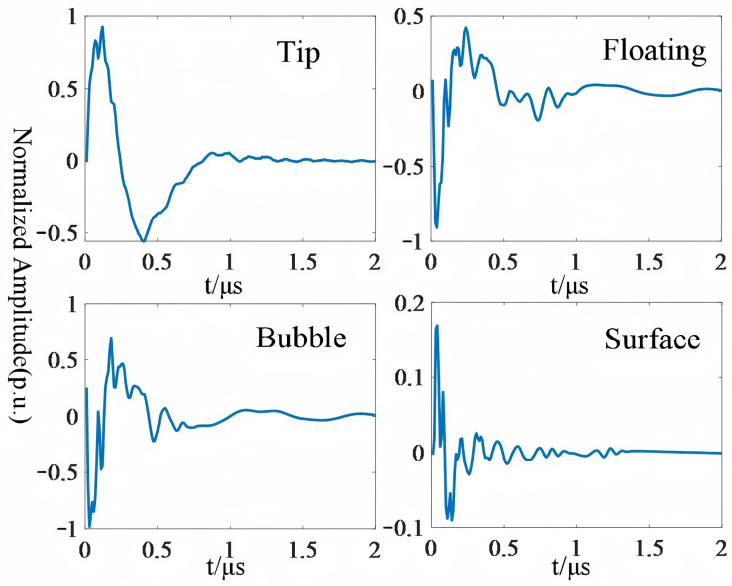

Figure 3. Four different waveforms of PD single pulse [21].

To replicate the characteristics of limited samples in the real PD signal dataset, the PD single-pulse samples for each discharge type were proportionally reduced to create

a training sample library. The distribution of each pulse type in the library is shown in Table 1.

Table 1. Sample distribution of PD pulse training sample datasets.

Type	Number of Training Set Pulse Samples	Number of Test Set Pulse Samples
Tip discharge	200	3000
Floating discharge	50	1200
Bubble discharge	120	2200
Surface discharge	80	1600

3. Data Augmentation and Pattern Recognition Method Based on DAE-GAN

3.1. Deep Self-Encoder and CWGAN-GP Model

The Deep Autoencoder (DAE) is based on the autoencoder architecture, with additional layers added to both the encoder and decoder to enhance their encoding and decoding capabilities. The DAE is optimized to minimize reconstruction error. The loss function for the DAE is defined in Equation (1).

$$\begin{cases} \hat{\boldsymbol{x}}_i = De[En(\boldsymbol{x}_i)] \\ loss_{DAE} = \sum_{i=1}^{n} \left(\boldsymbol{x}_i - \hat{\boldsymbol{x}}_i\right)^T \left(\boldsymbol{x}_i - \hat{\boldsymbol{x}}_i\right) \end{cases} \tag{1}$$

In Equation (1), En and De represent the encoding and decoding functions, respectively, while x_i and x_i denote the original data and the reconstructed data, respectively.

CWGAN-GP is an enhanced version of GAN, utilizing the Wasserstein distance as its objective function and incorporating a gradient penalty to enforce the 1-Lipschitz condition [25]. This addresses issues such as multi-class generation, gradient vanishing, and mode collapse in GANs. The CWGAN-GP loss function is presented in Equation (2).

$$\begin{cases} L_G = -E_{z\sim P_z}[D(G(\boldsymbol{z}|\boldsymbol{c})|\boldsymbol{c})] \\ L_D = E_{z\sim P_z}[D(G(\boldsymbol{z}|\boldsymbol{c})|\boldsymbol{c})] - \\ \qquad E_{\boldsymbol{x}\sim P_r}[D(\boldsymbol{x}|\boldsymbol{c})] + GP|_{\hat{\boldsymbol{x}}} \\ GP|_{\hat{\boldsymbol{x}}} = \lambda E_{\hat{\boldsymbol{x}}\sim P_{\hat{x}}}\left[\left(\left\|\nabla_{\hat{\boldsymbol{x}}} D\left(\hat{\boldsymbol{x}}\middle|\boldsymbol{c}\right)\right\|_p - 1\right)^2\right] \end{cases} \tag{2}$$

In Equation (5), L_G represents the generator loss function, L_D represents the discriminator loss function, P_z denotes the prior distribution of the random noise z, $GP|_{\hat{x}}$ is the gradient penalty term, and λ is the regularization coefficient.

The network structures of the DAE and CWGAN-GP are shown in Figure 4:

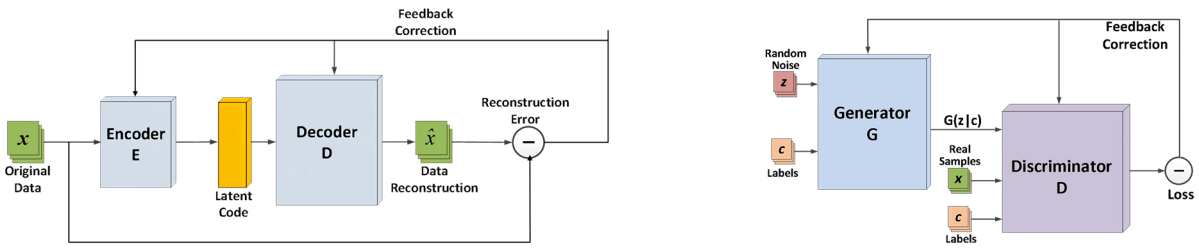

(**a**) DAE structure diagram (**b**) CWGAN-GP structure diagram

Figure 4. Structure diagrams of DAE and CWGAN-GP.

3.2. DAE-GAN Network and Its Training Process

The DAE is incorporated into the GAN's sample generation process to impose constraints, enhancing the authenticity of the generated data. A strong inverse relationship exists between a set and its complementary set, allowing the latter to provide additional probabilistic information for the same class. During the generation process, samples from other classes are introduced as complementary data to further enhance the process. The DAE-GAN network structure is depicted in Figure 5 [21], with red dashed lines showing the flow of generated data.

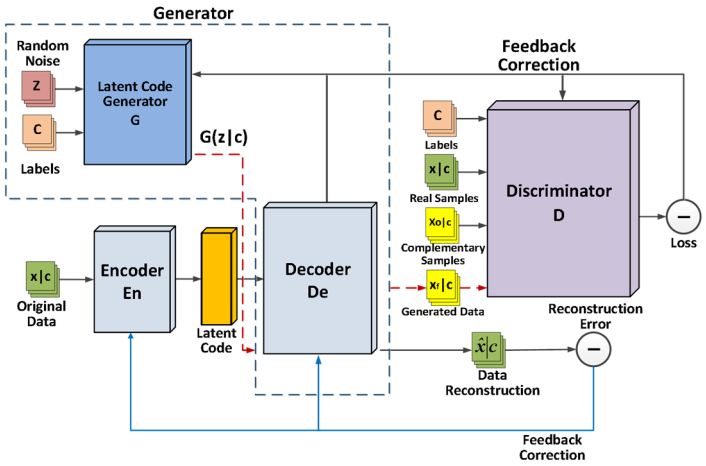

Figure 5. Structure diagram of DAE-GAN [21].

In DAE-GAN, the generator not only improves the quality of generated data through the constraints of the DAE but also introduces complementary data to provide an additional reference for minority classes. This mechanism allows the generator to produce diverse, high-quality samples even in data-scarce scenarios, thereby enhancing the generalization for minority class samples. With its strengths in noise reduction, increasing sample diversity, addressing data imbalance, and handling small-sample challenges, DAE-GAN is particularly suited for managing limited and unevenly distributed partial discharge samples in electrical equipment.

The CWGAN-GP models serve as the basis for sample generation. Since $\boldsymbol{x_r}$, $\boldsymbol{y}$, and $\boldsymbol{x_o}$ are in the same space, they share a common distance–cost function. Consequently, the Kantorovich–Rubinstein dual form [26] of the Wasserstein distance in CWGAN-GP is given in Equation (3).

$$\begin{cases} W(P_r, P_g) = \max\limits_{\|D\|_L \le 1} E[D(\boldsymbol{x}_r|\boldsymbol{c})] - \\ \qquad\qquad E[D(G(\boldsymbol{z}|\boldsymbol{c})|\boldsymbol{c})] \\ W(P_r, P_o) = \max\limits_{\|D\|_L \le 1} E[D(\boldsymbol{x}_r|\boldsymbol{c})] - \\ \qquad\qquad E[D(\boldsymbol{x}_o|\boldsymbol{c})] \end{cases} \tag{3}$$

Using the discriminator D as the distance–cost function, the generative network should satisfy both distance equations in Equation (3) simultaneously [27]. The decoder must also both deceive the discriminator and satisfy Equation (1). The loss functions for each module are provided in Equation (4).

In Equations (4) and (5), L_{En}, L_{De}, L_D, and L_G represent the loss functions for the encoder, decoder, discriminator, and latent code generator, respectively. γ_1 and γ_2 are adaptive coefficients for multi-objective functions, balancing the optimization progress between the discriminator and decoder to prevent mode collapse. β_1 and β_2 are set to 1×10^{-10} to avoid division by zero, which could cause algorithm failure. L_{margin} represents

the reconstruction error penalty, ensuring the error is not dominated by the gradient. M is the penalty factor, ma is the reconstruction error margin, and $\max\{\cdot\}$ is the max function.

$$\begin{cases} L_{En} = \min\limits_{En} \sum\limits_{i=1}^{n} \left(\boldsymbol{x}_{ri} - \hat{\boldsymbol{x}}_{ri}\right)^T \left(\boldsymbol{x}_{ri} - \hat{\boldsymbol{x}}_{ri}\right) \\ L_{De} = \min\limits_{De} M \cdot L_{margin} - \gamma_2 E_{z\sim P_z}\left[D\left(x_f \middle| \boldsymbol{c}\right)\right] + \\ \qquad \sum\limits_{i=1}^{n} \left(\boldsymbol{x}_{ri} - \hat{\boldsymbol{x}}_{ri}\right)^T \left(\boldsymbol{x}_{ri} - \hat{\boldsymbol{x}}_{ri}\right) \\ L_D = \min\limits_{D}\{-(1+\gamma_1) E_{\boldsymbol{x}_r\sim P_r}[D(\boldsymbol{x}_r|\boldsymbol{c})] + \\ \qquad \gamma_1 E_{\boldsymbol{x}_o\sim P_o}[D(\boldsymbol{x}_o|\boldsymbol{c})] + \\ \qquad E_{z\sim P_z}\left[D\left(x_f \middle| \boldsymbol{c}\right)\right]\} \\ L_G = \min\limits_{G}\left\{-E_{z\sim P_z}\left[D\left(x_f \middle| \boldsymbol{c}\right)\right]\right\} \end{cases} \tag{4}$$

where

$$\begin{cases} x_f = De(G(\boldsymbol{z}|\boldsymbol{c})) \\ \mathrm{dis}_1 = E_{\boldsymbol{x}_r\sim P_r}[D(\boldsymbol{x}_r|\boldsymbol{c})] - E_{z\sim P_z}\left[D\left(x_f \middle| \boldsymbol{c}\right)\right] \\ \mathrm{dis}_2 = E_{\boldsymbol{x}_r\sim P_r}[D(\boldsymbol{x}_r|\boldsymbol{c})] - E_{\boldsymbol{x}_o\sim P_o}[D(\boldsymbol{x}_o|\boldsymbol{c})] \\ \gamma_1 = \sqrt{\frac{\{\mathrm{dis}_1\}^2}{\{\mathrm{dis}_2\}^2 + \beta_1}} \\ \gamma_2 = \sqrt{\frac{\left[\sum\limits_{i=1}^{n}\left(\boldsymbol{x}_{ri} - \hat{\boldsymbol{x}}_{ri}\right)^T\left(\boldsymbol{x}_{ri} - \hat{\boldsymbol{x}}_{ri}\right)\right]^2}{E_{z\sim P_z}\left[D\left(x_f|\boldsymbol{c}\right)\right]^2 + \beta_2}} \\ L_{margin} = \max\left\{\sum\limits_{i=1}^{n}\left(\boldsymbol{x}_{ri} - \hat{\boldsymbol{x}}_{ri}\right)^T\left(\boldsymbol{x}_{ri} - \hat{\boldsymbol{x}}_{ri}\right) - ma, \quad 0\right\} \end{cases} \tag{5}$$

In Equation (4), both L_{En} and L_{De} include $\sum\limits_{i=1}^{n}(x_{ri} - \hat{x}_{ri})^T(x_{ri} - \hat{x}_{ri})$. This section is dedicated to mapping the decoder from low-dimensional latent vectors to their corresponding high-dimensional sample vectors. The primary objective of this process is to ensure that the generated samples closely resemble real ones by minimizing any discrepancies between them, thus enhancing the overall authenticity and accuracy of the generated data.

The training process of the DAE-GAN network is as follows:

Step 1: Begin by pre-training the DAE network with real samples, and establish the reconstruction error obtained at the conclusion of pre-training as the threshold for further processing.

Step 2: Optimize the network modules based on Equation (4).

Step 3: Repeat Step 2 until the GAN reaches Nash equilibrium, then stop the iterations.

3.3. Algorithm Workflow

The DAE-GAN network has the capability to generate PD time-domain samples, and its discriminator, following transfer learning, is able to recognize partial discharge patterns. Figure 6 illustrates the framework used for partial discharge data augmentation and pattern recognition through the DAE-GAN model. The key steps involved in this process are outlined as follows:

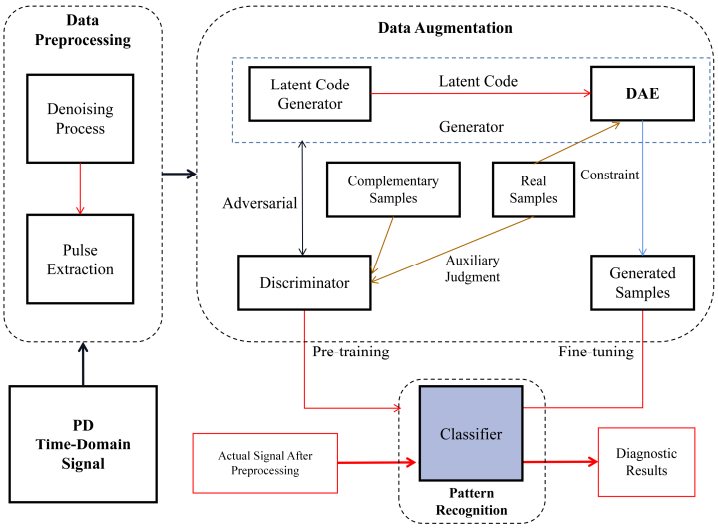

Figure 6. Data augmentation and pattern recognition for PD signals based on DAE-GAN.

Step 1: Data preprocessing. Apply wavelet denoising to the 20 ms PD signals and segment the pulses to create the training sample library for different types of PD signals as outlined in Table 1.

Step 2: Data augmentation. Input the training samples into the DAE-GAN network and proceed with training. Use the trained generator (G) and decoder (De) to generate varying quantities of samples based on the original data imbalance, expanding the training sample library.

Step 3: Partial discharge pattern recognition. Fine-tune the classifier D trained in Step 2 using the augmented training sample library. Use the average value between the minimum classification score for samples of the same class and the maximum classification score for samples of other classes as the classification criterion. Input the PD pulses extracted during actual operation into the classifier D for recognition.

4. Case Analysis

4.1. Subsection

After extensive testing, it was found that setting the latent code dimension to 13 yields minimal reconstruction error upon convergence. With this result, the structure and parameters of each module within the DAE-GAN network have been established accordingly, as detailed in Table 2.

Table 2. Network structure and parameter setting.

Network Module		Type	Number of Channels	Activation Function
Encoder		Fully connected layer × 5	200-5000-5000-4000-13	LeakyReLU
Generator	Decoder	Fully connected layer × 5	13-4000-5000-5000-200	Tanh
	Latent code generator	Fully connected layer × 5	13-500-1000-500-13	ReLU
Discriminator		Fully connected layer × 4	200-5000-400-1	ReLU

Hardware Environment: Desktop computer (Windows 10 operating system, CPU model: AMD Ryzen 5 3600, GPU model: 1660 Super Ultra).

Software Environment: The model development was carried out in the PyTorch framework. The Adam optimizer was employed for optimization, with learning rates

configured at 5×10^{-6} for both the encoder and decoder, while the momentum factors were set to 0.9 and 0.99, respectively. As for the discriminator and latent code generator, the learning rates were adjusted to 5×10^{-5}, with momentum factors of 0.5 and 0.9. The pre-training phase consisted of 2000 iterations, followed by 5000 iterations for training the complete DAE-GAN network.

4.2. Evaluation of Data Augmentation Capability of the DAE-GAN Model

The effectiveness of data augmentation in the DAE-GAN model is dependent on its ability to generate samples, which is primarily evaluated by the authenticity of the generated data and how well the probability distributions are fitted. To provide a clear comparison of the model's generative capabilities, this study contrasts it with three other models: CWGAN-GP, BEGAN, and VAE. The performance of these models is assessed based on two main factors: the diversity of the samples generated and their similarity to real-world samples. Each of these models was trained using the sample library data presented in Table 1.

4.2.1. Evaluation of Similarity of Generated Samples by the Model

As shown in Figure 7, the four types of PD waveforms: tip discharge, floating discharge, bubble discharge, and surface discharge are presented. A real sample was randomly selected, and the correlation coefficient was employed as the evaluation criterion. For comparison, the PD pulse time–domain waveform with the highest similarity to the real sample, generated by each model, was chosen based on this criterion.

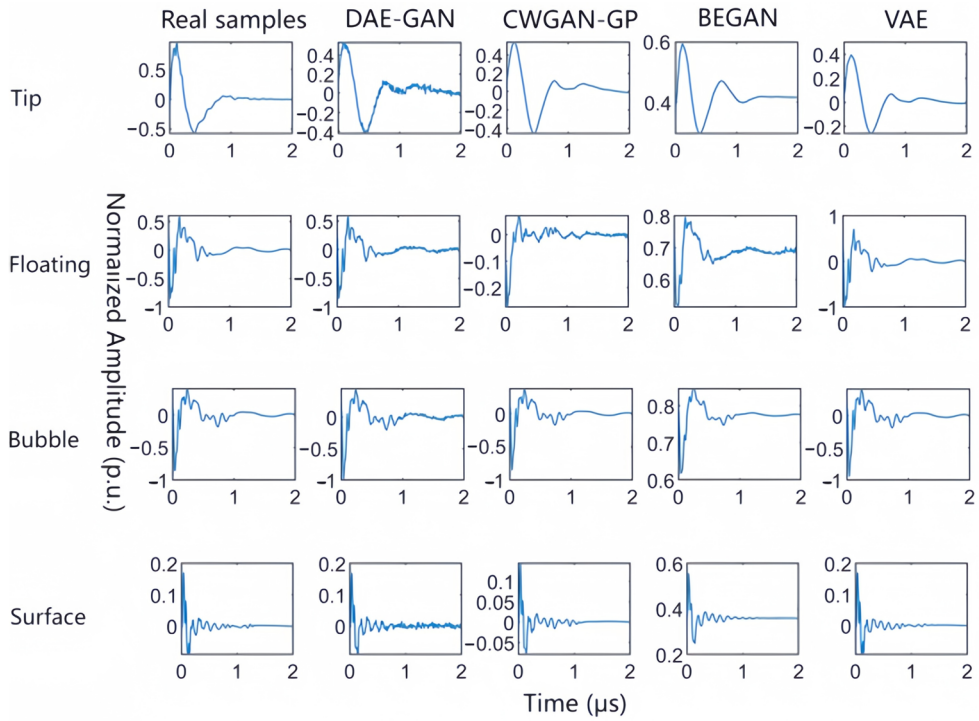

Figure 7. Comparison of PD waveforms generated by different models.

As observed in Figure 7, both BEGAN and VAE generate relatively smooth samples; however, VAE loses some of the original sample's fluctuations. The waveform generated by CWGAN-GP contains some noise-like fluctuations. In contrast, the samples generated by DAE-GAN are also relatively smooth and do not suffer from the issue of losing parts of the original sample's fluctuations, as seen with VAE.

The aforementioned real sample and the PD samples generated by each model were subjected to FFT transformation [28], with a time window length of 137 sampling points to obtain two-dimensional time-frequency diagrams for each sample. For a quantitative

assessment of the similarity between the time–frequency diagrams, the Multi-scale Structural Similarity (MS-SSIM) [29] metric was employed. This method measures the visual similarity between two images at different scales, where a higher MS-SSIM value signifies a greater resemblance between the two samples. The detailed comparison results obtained from this analysis are provided in Table 3.

Table 3. MS-SSIM index of different models.

	Tip Discharge	Floating Discharge	Bubble Discharge	Surface Discharge	MS-SSIM Mean Value
CWGAN-GP	0.9175	0.9449	0.9732	0.9728	0.9521
BEGAN	0.9197	0.7932	0.9995	0.9551	0.9169
VAE	0.8470	0.9023	0.956	0.9383	0.9109
DAE-GAN	0.9504	0.9993	0.9995	0.9763	0.9814

As shown in Table 3, the MS-SSIM values for the samples generated by VAE are generally lower due to the loss of some fluctuations. For BEGAN, the MS-SSIM value is the lowest for the floating discharge waveform because of mode collapse. The MS-SSIM values and mean MS-SSIM values for the waveforms generated by DAE-GAN are the highest for all types of discharge, indicating the highest similarity between its generated waveforms and the original samples.

4.2.2. Evaluation of Model-Generated Sample Diversity and Distribution Similarity

Taking surface discharge as an illustrative example, the t-distributed stochastic neighbor embedding (t-SNE) algorithm [30] was utilized to perform dimensionality reduction on both real samples and a selection of generated samples from each model. This method allows for visualizing the high-dimensional data in a more interpretable, low-dimensional space. The resulting visual representations of these samples are provided in Figure 8.

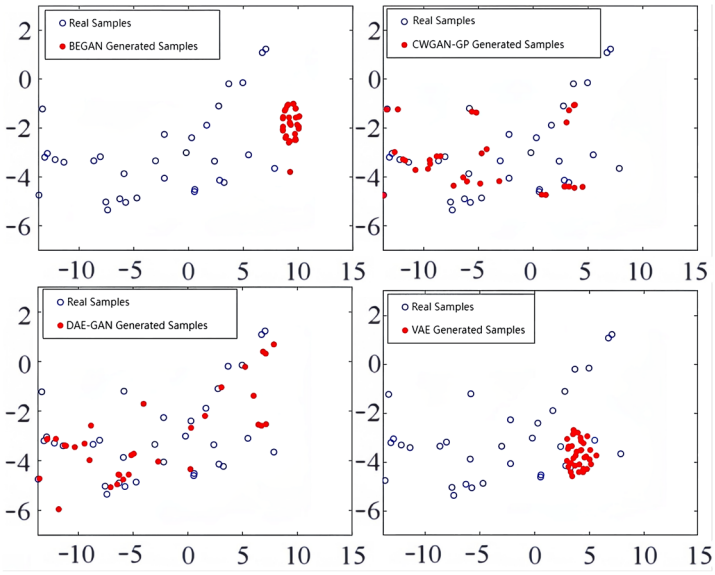

Figure 8. The dimension reduction results of PD samples.

As clearly shown in Figure 8, both BEGAN and VAE models experienced mode collapse, with the generated samples concentrated in a small area near the real samples. In contrast, CWGAN-GP and DAE-GAN, which account for the 1-Lipschitz continuity condition, have their generated samples scattered within the distribution range of the real samples, indicating better diversity.

While diversity gives an indication of variety, another crucial aspect of generative model evaluation is how well the generated samples align with the original data's underlying distribution. A well-performing generative model should not only produce diverse samples but also accurately replicate the statistical properties of the real data. In this context, examining the probability distribution of the generated samples provides deeper insights into how closely the model captures the real data structure. Therefore, it is essential to assess not only the spread of the generated samples but also their probability density relative to the original dataset.

The generative capability of a model is primarily reflected in the accuracy of fitting the original distribution. Evaluating model performance solely based on diversity has certain limitations. Using the 'ksdensity' function in MATLAB to approximate the distribution of the dimensionally reduced samples, the probability distributions of the real samples and the generated samples from each model are compared in Figure 9. The 3D probability distribution plot illustrates the distribution of samples after dimensionality reduction. The *X*-axis and *Y*-axis represent the two dimensions of the samples, while the *Z*-axis and color indicate the probability density of the samples at different positions. This visualization helps to intuitively display the distribution characteristics and correlations between variables.

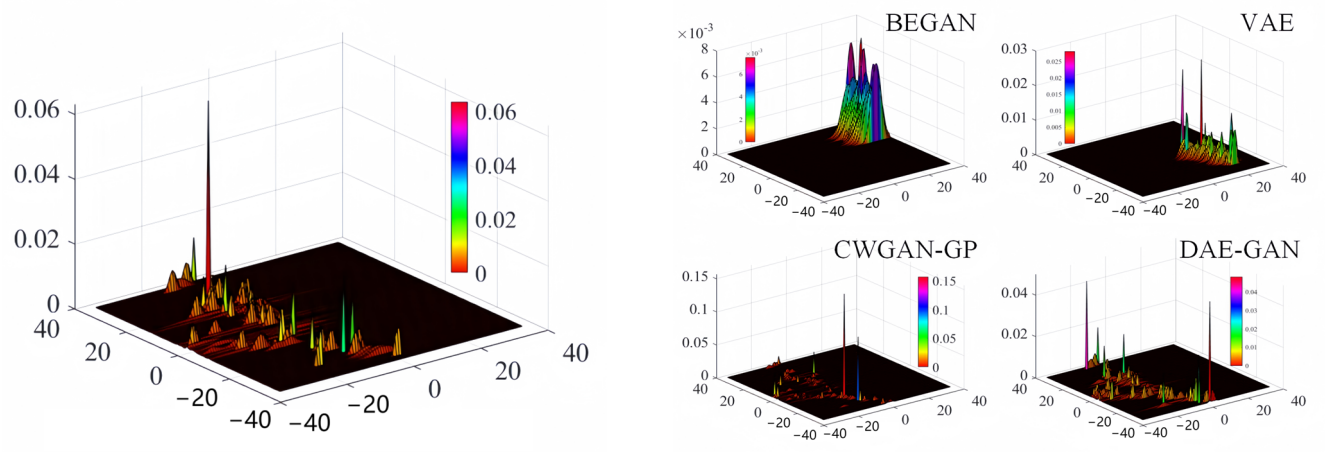

(a) Probability distribution of real samples **(b)** Probability distribution of generated samples by each model

Figure 9. Probability distribution of dimension reduction samples of local emission signals.

A comparison of subfigures (a) and (b) in Figure 9 shows that the probability distributions of samples generated by BEGAN and VAE are confined to specific regions, displaying significant differences from the distribution of real samples. While CWGAN-GP generates probabilities closer to the real samples, some small areas exhibit excessively high probabilities. The 3D visualizations reveal that the probability distribution of samples generated by DAE-GAN closely aligns with that of real samples. The reason is that the autoencoder first reduces the dimensionality of the original samples and then maps them back to the high-dimensional sample space. This two-step process allows the model to preserve the essential features of the original data while effectively reconstructing them in higher dimensions. As a result, the generated samples maintain key characteristics of the real data, leading to a probability distribution that more accurately reflects that of the original samples.

After converting the 3D probability distribution plots into 2D grayscale images and applying a zero-removal process, the similarity between the probability distribution of the generated partial discharge samples and the real samples was assessed. This evaluation was done using the Multi-Scale Structural Similarity Index (MS-SSIM). Higher MS-SSIM values indicate greater similarity between the generated and real sample distributions. The

specific MS-SSIM values calculated for each model are summarized in Table 4, providing a clear comparison of how closely each model's generated samples align with the actual data.

Table 4. MS-SSIM index of probability distribution of different models.

Model	CWGAN-GP	BEGAN	VAE	DAE-GAN
MS-SSIM values	0.8463	0.7979	0.7838	0.8680

As shown in Table 4, the MS-SSIM values for BEGAN and VAE are clearly lower than those of the other two models. The DAE-GAN model has the highest MS-SSIM value, indicating the highest fitting accuracy of the probability distribution for the generated partial discharge samples.

4.3. Analysis of Network Data Augmentation and Pattern Recognition Effectiveness

To comprehensively assess the effectiveness of the proposed data augmentation method across various classifiers and evaluate its influence on classification accuracy, a multi-class evaluation framework based on the confusion matrix was employed. This approach provides a thorough examination of the method's performance in enhancing classification outcomes. The formulas for calculating classification accuracy ($\lambda_{accuracy}$%), F1 score (λ_{F1}%), and G-mean ($\lambda_{G\text{-}mean}$%) are provided in reference [31].

4.3.1. Applicability of DAE-GAN

To evaluate the applicability of the data augmentation method proposed, a Support Vector Machine (SVM) [32] with a radial basis function kernel and a classifier network structure of 13-5000-400-1 sparse autoencoder (SAE) [33] were included for comparison. The classifiers were trained using both the original sample set and the sample set expanded with DAE-GAN generated samples. Following the training phase, the classifiers were utilized to conduct pattern recognition analysis on partial discharge signals, and the evaluation metrics are compared in Table 5.

Table 5. Comparison of classification effect before and after data augmentation.

Classifier	$\lambda_{accuracy}$%		λ_{F1}%		$\lambda_{G\text{-}mean}$%	
	Before Augmentation	After Augmentation	Before Augmentation	After Augmentation	Before Augmentation	After Augmentation
SVM	78.74	88.89	77.92	88.25	78.20	88.33
SAE	87.51	91.05	85.56	92.59	87.83	92.88
Classifier used	90.12	98.36	88.62	97.82	89.93	97.62

In Table 5, $\lambda_{accuracy}$%, λ_{F1}%, and $\lambda_{G\text{-}mean}$% represent three common metrics used to evaluate machine learning models in classification tasks, each with a distinct focus, especially in the context of imbalanced datasets. $\lambda_{accuracy}$% is a widely used metric for evaluating classification models, reflecting the ratio of correctly classified samples to the total sample size. It is particularly effective when the dataset has a relatively balanced distribution of positive and negative samples. λ_{F1}% is a metric that combines Precision and Recall, calculated as the harmonic mean of these two metrics. It is particularly useful for evaluating model performance on imbalanced datasets, where the focus is on balancing Precision and Recall. $\lambda_{G\text{-}mean}$%, on the other hand, is specifically designed for imbalanced datasets, measuring the model's balance between positive and negative class performance. It is particularly effective in situations where the dataset is highly imbalanced. The selection of these three metrics for evaluating model performance is based on their distinct focuses, which are suitable for different data distributions and task requirements. In particular, they offer a comprehensive evaluation of model performance in classification tasks with

imbalanced datasets, each providing a unique perspective. This helps to avoid the bias of relying on a single metric, thereby enhancing the credibility of the evaluation results.

By comparing the evaluation metrics of each classifier before and after data augmentation in Table 5, it is evident that all classifiers show an improvement in their evaluation metrics after DAE-GAN data augmentation. This demonstrates that the proposed data augmentation method is effective and applicable across various classifiers, including SVM and SAE, as well as the specific classifier utilized in this study.

4.3.2. Comparison of Classification Effectiveness of Different Data Augmentation Methods

To verify the effectiveness of the proposed data augmentation method for partial discharge pulse samples, five oversampling techniques—ROS, SMOTE, CWGAN-GP, BEGAN, and VAE—were selected for comparison. Each of these methods, along with the proposed sample generation approach, was used to balance and expand the capacity of each partial discharge sample type to 1500. The classifier used was then trained using the different augmented sample libraries. The evaluation metrics for the classifier trained on the original samples and on the samples augmented using different oversampling methods are shown in Table 6.

Table 6. Comparison of classification effects with different data augmentation techniques.

Data Augmentation Methods	$\lambda_{accuracy}$%	λ_{F1}%	$\lambda_{G\text{-}mean}$%
Original samples	90.12	88.62	89.93
ROS	89.04	87.54	88.85
SMOTE	96.38	95.88	93.94
CWGAN-GP	97.57	97.58	97.20
BEGAN	97.17	97.06	96.81
VAE	96.77	96.47	94.75
DAE-GAN	98.36	97.82	97.62

As shown in Table 6, the classifier trained on the original samples exhibits low recognition accuracy due to the imbalance and small size of the partial discharge dataset. ROS does not significantly improve classification performance. While SMOTE, BEGAN, and VAE can enhance performance, their effects are moderate. CWGAN-GP produces more diverse samples, resulting in a greater improvement in classification accuracy. After DAE-GAN data augmentation, the accuracy, F1 score, and G-mean metrics are improved by 8.24%, 9.20%, and 7.69%, respectively, compared to the pattern recognition metrics trained on the original samples. The classification accuracy also shows varying degrees of improvement compared to other data augmentation algorithms.

4.4. Analysis of the Role of Introducing Complementary Samples

To assess the impact of incorporating complementary samples into the generative model's training process, the model was trained under two different conditions: one without the inclusion of complementary samples and the other with these additional samples. This comparative approach helps highlight the effectiveness of introducing complementary data in enhancing the model's performance.

By introducing a population diversity metric [34], as shown in Equation (6), the diversity of the model-generated samples is quantitatively evaluated. In Equation (6), $loss_{div}$ represents the diversity cost function, Ω denotes the set of real and generated samples, $\|K\|$ refers to the maximum diagonal distance in the space of Ω, and m is the total number of elements in the set.

$$loss_{div} = \frac{1}{m\|K\|} \sum_{\boldsymbol{u} \in \Omega} \sqrt{\left(\boldsymbol{u} - \bar{\boldsymbol{u}}\right)^{T} \left(\boldsymbol{u} - \bar{\boldsymbol{u}}\right)} \tag{6}$$

Following the method outlined in Section 4.3.2, the diversity variation plots for different sample sizes and the MS-SSIM metrics of the probability distribution images were obtained, as shown in Figure 10 and Table 7.

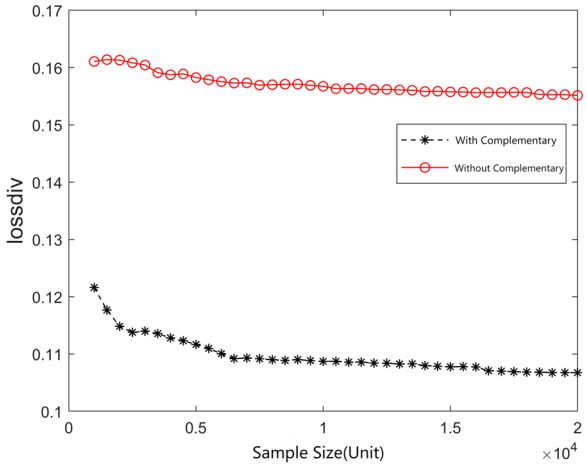

Figure 10. Diversity comparison of samples generated by models under different conditions.

Table 7. MS-SSIM metrics for probability distribution maps under different conditions.

Metrics	Without Complementary Samples	With Complementary Samples
MS-SSIM value	0.8492	0.8680

As shown in Figure 10, the diversity evaluation metric for PD samples generated by DAE-GAN is consistently higher when complementary samples are included in the training compared to when they are not. The inclusion of complementary samples effectively enhances the diversity of the generated samples. From Table 7, it is evident that the MS-SSIM values of the probability distribution images are significantly higher when complementary samples are included in the DAE-GAN training. This indicates that the inclusion of complementary samples effectively improves the fitting accuracy of the probability distribution and can effectively mitigate the issue of insufficient probabilistic information caused by the small sample characteristics of partial discharge data.

The DAE-GAN model was employed to augment the sample data under both experimental conditions, one without and one with complementary samples. These augmented datasets were then utilized to train the classifier for conducting pattern recognition tasks. The performance evaluation metrics derived from these experiments are detailed in Table 8.

Table 8. Comparison of classification effects with complementary samples.

Data Augmentation Method	$\lambda_{accuracy}$%	λ_{F1}%	$\lambda_{G\text{-}mean}$%
Without complementary samples	97.21	96.50	96.50
With complementary samples	98.36	97.82	97.62

As shown in Table 8, when complementary samples are included, all classification performance evaluation metrics for the classifier trained with the augmented samples from the generative model are higher than when complementary samples are not included. The $\lambda_{accuracy}$%, λ_{F1}%, and $\lambda_{G\text{-}mean}$% improved by 1.15%, 1.32%, and 1.12%, respectively. This demonstrates that the inclusion of complementary samples effectively enhances the classification performance.

5. Conclusions

To address the issue of low accuracy in partial discharge pattern recognition caused by imbalanced and limited sample sizes, this study proposes a novel approach combining data augmentation with pattern recognition using DAE-GAN. The key findings of the study are summarized as follows:

(1) When assessed using the key criteria of authenticity, sample diversity, and the accuracy with which the model fits the probability distribution, the DAE-GAN model demonstrates a clear advantage in generative capability. It outperforms other models, such as BEGAN, VAE, and CWGAN-GP, in these aspects, making it a more robust choice for generating high-quality samples.

(2) After data augmentation with DAE-GAN, the pattern recognition accuracy indicators, $\lambda_{accuracy}$%, λ_{F1}%, and $\lambda_{G\text{-}mean}$%, increased by 8.24%, 9.20%, and 7.69%, respectively, compared to the pattern recognition trained on the original samples. This effectively improves the accuracy of partial discharge pattern recognition. Additionally, the accuracy after DAE-GAN data augmentation is higher compared to other data augmentation algorithms included in the comparison.

(3) The sample generation capability of DAE-GAN is enhanced by including complementary samples, effectively addressing the issue of insufficient probabilistic information caused by the small sample characteristics of partial discharge. Compared to when no complementary samples are included, the $\lambda_{accuracy}$%, λ_{F1}%, and $\lambda_{G\text{-}mean}$% indicators improved by 1.15%, 1.32%, and 1.12%, respectively. The inclusion of complementary samples effectively improves classification performance.

The current DAE-GAN model still has several areas for improvement, particularly in terms of the collaborative training between the DAE and GAN modules. Further in-depth research is required to effectively coordinate the training processes of both modules to achieve complementary and enhanced performance. Moreover, the hyperparameters of the current model are determined through experimental adjustment, which may not be optimal for different datasets and tasks. Therefore, designing an adaptive mechanism that can dynamically adjust hyperparameters to meet the needs of various training stages, while optimizing the training process and improving overall model performance, remains a crucial challenge to be addressed.

Author Contributions: Conceptualization, J.X.; Data curation, Z.S. and C.W.; Formal analysis, C.W.; Funding acquisition, X.D.; Methodology, X.D. and J.X.; Validation, X.D., J.Q., J.K. and J.X.; Writing—original draft, X.D. All authors have read and agreed to the published version of the manuscript.

Funding: This research received financial support from the Science and Technology Projects of Inner Mongolia Electric Power (Group) Co., Ltd.

Informed Consent Statement: Not applicable.

Data Availability Statement: The raw data supporting the conclusions of this article will be made available by the authors upon request.

Acknowledgments: We are thankful to the anonymous reviewers for their insightful comments, which have significantly contributed to improving the quality of this paper. The authors also express their gratitude to North China Electric Power University for their support in the publication of this article. Special thanks are extended to Inner Mongolia Electric Power (Group) Co., Ltd. Alxa Power Supply Branch for their valuable assistance and support during the research process.

Conflicts of Interest: Author Xin Du, Jun Qi, Jiyi Kang were employed by the company Alxa Power Supply Branch, Inner Mongolia Electric Power (Group) Co., Ltd. The remaining authors declare that the research was conducted in the absence of any commercial or financial relationships that could be construed as a potential conflict of interest.

References

1. da Silva, A.M.L.; Araújo, L.F. Reliability evaluation of generating systems considering aging processes. *Electr. Power Syst. Res.* **2022**, *202*, 107589. [CrossRef]
2. Garip, S.; Özdemir, Ş.; Altın, N. Power System Reliability Assessment—A Review on Analysis and Evaluation Methods. *J. Energy Syst.* **2022**, *6*, 401–419. [CrossRef]
3. Eltamaly, A.M.; Mohamed, Y.S.; El-Sayed, A.H.M.; Elghaffar, A.N.A. Advanced Control Techniques for Enhance the Power System Stability at OOS Condition. *Insight-Energy Sci.* **2019**, *2*, 89. [CrossRef]
4. Hussain, G.A.; Hassan, W.; Mahmood, F.; Shafiq, M.; Rehman, H.; Kay, J.A. Review on partial discharge diagnostic techniques for high voltage equipment in power systems. *IEEE Access* **2023**, *11*, 51382–51394. [CrossRef]
5. Long, B.; Yu, K.; Qin, J.Y. Data Augmentation for Unbalanced Face Recognition Training Sets. *Neurocomputing* **2017**, *235*, 10–14. [CrossRef]
6. Chang, Z.; Wu, J.; Liang, H.; Wang, Y.; Wang, Y.; Xiong, X. A Review of Power System False Data Attack Detection Technology Based on Big Data. *Information* **2024**, *15*, 439. [CrossRef]
7. Bean, W.T.; Stafford, R.; Brashares, J.S. The effects of small sample size and sample bias on threshold selection and accuracy assessment of species distribution models. *Ecography* **2012**, *35*, 250–258. [CrossRef]
8. Lv, F.; Liu, G.; Wang, Q.; Lu, X.; Lei, S.; Wang, S.; Ma, K. Pattern recognition of partial discharge in power transformer based on infogan and cnn. *J. Electr. Eng. Technol.* **2023**, *18*, 829–841. [CrossRef]
9. Shorten, C.; Khoshgoftaar, T.M.; Furht, B. Text data augmentation for deep learning. *J. Big Data* **2021**, *8*, 101. [CrossRef]
10. Mohammed, R.; Rawashdeh, J.; Abdullah, M. Machine learning with oversampling and undersampling techniques: Overview study and experimental results. In Proceedings of the 2020 11th International Conference on Information and Communication Systems (ICICS), Irbid, Jordan, 7–9 April 2020; pp. 243–248.
11. Batista, G.E.; Prati, R.C.; Monard, M.C. A study of the behavior of several methods for balancing machine learning training data. *ACM Sigkdd Explor. Newsl.* **2004**, *6*, 20–29. [CrossRef]
12. Xu, Z.; Shen, D.; Kou, Y.; Nie, T. A synthetic minority oversampling technique based on Gaussian mixture model filtering for imbalanced data classification. *IEEE Trans. Neural Netw. Learn. Syst.* **2022**, *35*, 3740–3753. [CrossRef] [PubMed]
13. Qiao, Y.; Zhang, W.; Tian, Z.; Yang, L.T.; Liu, Y.; Alazab, M. Adversarial malware sample generation method based on the prototype of deep learning detector. *Comput. Secur.* **2022**, *119*, 102762. [CrossRef]
14. Cao, J.; Ma, J.; Huang, D.; Yu, P.; Wang, J.; Zheng, K. Method to enhance deep learning fault diagnosis by generating adversarial samples. *Appl. Soft Comput.* **2022**, *116*, 108385. [CrossRef]
15. Yang, H.; Qiu, R.C.; Shi, X.; He, X. Unsupervised feature learning for online voltage stability evaluation and monitoring based on variational autoencoder. *Electr. Power Syst. Res.* **2020**, *182*, 106253. [CrossRef]
16. Kossale, Y.; Airaj, M.; Darouichi, A. Mode collapse in generative adversarial networks: An overview. In Proceedings of the 2022 8th International Conference on Optimization and Applications (ICOA), Genoa, Italy, 6–7 October 2022; pp. 1–6.
17. Berthelot, D.; Schumm, T.; Metz, L. BEGAN: Boundary equilibrium generative adversarial networks. *arXiv* **2017**, arXiv:1703.10717.
18. Zheng, M.; Li, T.; Zhu, R.; Tang, Y.; Tang, M.; Lin, L.; Ma, Z. Conditional Wasserstein generative adversarial network-gradient penalty-based approach to alleviating imbalanced data classification. *Inf. Sci.* **2020**, *512*, 1009–1023. [CrossRef]
19. Shao, H.; Jiang, H.; Zhao, H.; Wang, F. A novel deep autoencoder feature learning method for rotating machinery fault diagnosis. *Mech. Syst. Signal Process.* **2017**, *95*, 187–204. [CrossRef]
20. Lemke, E. A critical review of partial-discharge models. *IEEE Electr. Insul. Mag.* **2012**, *28*, 11–16. [CrossRef]
21. Dong, C.; Pang, X.; Lu, S.; Zhao, J.; Liu, Z.; Xie, J. Partial Discharge Data Augmentation and Pattern Recognition for Unbalanced and Small Sample Scenarios. *J. Phys. Conf. Ser.* **2023**, *2477*, 012078. [CrossRef]
22. Rodrigo-Mor, A.; Muñoz, F.A.; Castro-Heredia, L.C. Principles of charge estimation methods using high-frequency current transformer sensors in partial discharge measurements. *Sensors* **2020**, *20*, 2520. [CrossRef]
23. Wen, B.; Li, Y.; Pfister, L.; Bresler, Y. Joint adaptive sparsity and low-rankness on the fly: An online tensor reconstruction scheme for video denoising. In Proceedings of the IEEE International Conference on Computer Vision, Venice, Italy, 22–29 October 2017; pp. 241–250.
24. Hua, C.; Wu, B.; Li, B.; Hua, X.; Geng, Y. A pressure pulse recognition method based on flow-adaptive double threshold for pressure pulse telemetry. *J. Pet. Sci. Eng.* **2023**, *220*, 111158. [CrossRef]
25. Gulrajani, I.; Ahmed, F.; Arjovsky, M.; Dumoulin, V.; Courville, A.C. Improved training of wasserstein gans. In Proceedings of the Conference on Neural Information Processing Systems, Long Beach, CA, USA, 4–9 December 2017; pp. 5767–5777.
26. Heinemann, F.; Klatt, M.; Munk, A. Kantorovich–rubinstein distance and barycenter for finitely supported measures: Foundations and algorithms. *Appl. Math. Optim.* **2023**, *87*, 4. [CrossRef]
27. Aparicio, J.; Pastor, J.T. A General Input Distance Function Based on Opportunity Costs. *Adv. Decis. Sci.* **2011**, *2011*, 505241. [CrossRef]
28. Rife, D.C.; Vincent, G.A. Use of the discrete Fourier transform in the measurement of frequencies and levels of tones. *Bell Syst. Tech. J.* **1970**, *49*, 197–228. [CrossRef]
29. Veras, R.; Collins, C. Discriminability tests for visualization effectiveness and scalability. *IEEE Trans. Vis. Comput. Graph.* **2020**, *26*, 749–758. [CrossRef] [PubMed]

30. Vinothini, N.; Aishwarya, S.; Kiruthika, D.; Ananthi, G. Intelligent Energy Transfer and Node Localization in the Internet of Things Using Deep Reinforcement Learning. In Proceedings of the 2023 International Conference on Energy, Materials and Communication Engineering (ICEMCE), Madurai, India, 14–15 December 2023; pp. 1–5.
31. Liu, H.; Ren, H.; Zheng, Z.; Wang, W.; Xia, J.; Yang, J. Transient Voltage Stability Assessment of Power System Based on Improved Deep Residual Network. *Mod. Electr. Power* **2023**, *40*, 879–889.
32. Pisner, D.A.; Schnyer, D.M. Support Vector Machine. In *Machine Learning*; Academic Press: Cambridge, MA, USA, 2020; pp. 101–121.
33. Al-Qatf, M.; Lasheng, Y.; Al-Habib, M.; Al-Sabahi, K. Deep learning approach combining sparse autoencoder with SVM for network intrusion detection. *IEEE Access* **2018**, *6*, 52843–52856. [CrossRef]
34. Riget, J.; Vesterstrom, J.S. *A Diversity-Guided Particle Swarm Optimizer—The ATPSO*; University of Aarhus Department of Computer Science: Aarhus, Denmark, 2002.